Sensorless Synchronous Motor Drives: A Review of Flux Observer-based Position Estimation Schemes using the Projection Vector Framework

Sensorless Synchronous Motor Drives: A Review of Flux Observer-based Position Estimation Schemes using the Projection Vector Framework

Anantaram Varatharajan, Gianmario Pellegrino, *Senior Member, IEEE,* Eric Armando, *Senior Member, IEEE,* and Marko Hinkkanen, *Senior Member, IEEE*

***Abstract*—This paper reviews six fundamental-wave excitation sensorless techniques for synchronous machines reported in the literature. All the techniques rely on a hybrid flux observer scheme, combining the voltage and current-models of the machine, and use the flux observer error signal to track the rotor phase angle and the rotational speed. A common mathematical framework with magnetic nonlinearity is constructed for the stability analysis where each of the studied technique is represented by a unique projection vector. The dynamics of the flux and the position observer is investigated and the regions of instability are identified for each scheme under similar operating conditions. Experimental validation to support the stability analysis is reported on a 1.1 kW synchronous reluctance (SyR) machine test-bench.**

***Index Terms*—Sensorless control, synchronous machine, projection vector framework, stability analysis.**

I. Introduction

Sensorless control of synchronous machines without a position transducer finds significance in automotive and industrial applications for cost reduction and reliability. Low speed sensorless control techniques rely on high-frequency excitation approach to exploit the differential saliency for position estimation. This comprises of two main categories: continuous excitation using periodic signal injection [1], [2] and discontinuous excitation schemes [3], [4]. In medium to high speed region, the fundamental-wave excitation approaches are preferred for reliability and absence of acoustic noise.

This work concerns the latter category of fundamental-wave excitation methods based on back-emf integration for position estimation at medium to high speeds region. This paper constructs a general mathematical framework for stability analysis to review six flux observer-based sensorless schemes in literature. The magnetic saturation in modern synchronous machines are significant and have been omitted in theoretical frameworks and comparisons in the existing literature. To fill the gap, this paper develops a projection vector framework based on the small-signal machine model accounting for the magnetic saturation. The framework allows a systematical stability analysis as well as improved gain selection for sensorless methods. In this work, the position error function ϵ of each of the considered schemes is represented as a projection of the difference in the observed and the current-model flux estimates, $\hat{\boldsymbol{\lambda}}_{\hat{d}\hat{q}} - \boldsymbol{\lambda}^{i}_{\hat{d}\hat{q}}$, along a unique vector $\boldsymbol{\phi}$, as shown in Fig. 1.

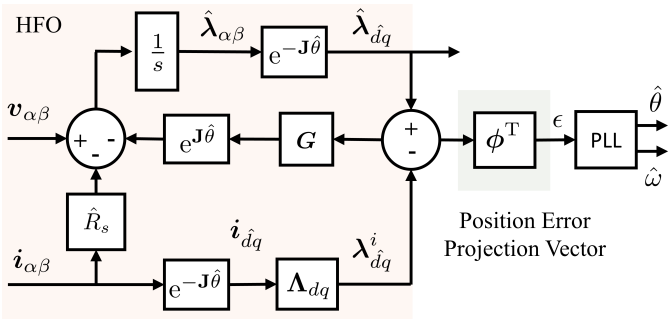

Fig. 1. Hybrid flux observer (HFO) with projection vector-based position error signal and a phase-locked-loop (PLL) for position tracking.

The six flux observer-based sensorless schemes for synchronous machines are: *(i)* Flux cross-product based position observer [5]–[7] where the position error function is proportional to the cross-product of the observed and the current-model estimates; *(ii)* Active-flux position observer [8]–[11] where the position error function is proportional to the q-axis component of the observed active-flux in the estimated rotor reference frame; *(iii)* Fundamental saliency-based position observer [12] where the position error function is extracted from the anisotropic component of the stator flux; *(iv)* Auxiliary-flux position observer [13] where the projection vector is designed along the observed auxiliary-flux vector; *(v)* Adaptive projection vector for position error estimation (APP) scheme [14], [15] where the projection vector is adapted such that the position error signal is equal to the position error in steady-state conditions; *(vi)* Adaptive-gain position observer [16], [17] where the flux observer gain is adapted such that the dynamics of the position and the flux observer are decoupled.

This is by no means an exhaustive review; only the subset of flux observer based schemes are candidate, namely the ones where the position information is retrieved from the difference between the back-emf integral model and the current model flux estimates, complying with the structure in Fig. 1. Among

This work was supported by the Power Electronics Innovation Center (PEIC) of Politecnico di Torino, Italy. *(Corresponding author: Anantaram Varatharajan)*

A. Varatharajan, G. Pellegrino and E. Armando are with the Department of Energy, Politecnico di Torino, Turin 10129, Italy. (email: anantaram.varatharajan@polito.it; gianmario.pellegrino@polito.it; eric.armando@polito.it)

M. Hinkkanen is with the Department of Electrical Engineering and Automation, Aalto University, Espoo FI-00076, Finland (email: marko.hinkkanen@aalto.fi)

others, a common fundamental-wave excitation sensorless scheme without flux observer is the extended back-emf approach [18]–[20]. Extended Kalman filter and sliding mode techniques are reported in [21]–[23]. Sensorless schemes based on the flux observer with current feedback are investigated in [24], [25] which are mathematically equivalent to Fig. 1 only for linear magnetic model (no saturation) with the gains scaled accordingly.

Section II presents the mathematical model and the flux observer analysis. Section III introduces the concept of projection vectors and develops a framework for stability analysis. Section IV contains the main contributions of the paper, enumerated as follows:

1) The six flux observer-based position observers under review are represented in a generalized form where each technique is characterized by a unique vector, under the common mathematical definition of projection vector.
2) The different schemes are subjected to an identical stability analysis to reveal regions of instability under similar operating conditions.
3) The stability analysis is validated with a control resistance perturbation test on a 1.1 kW synchronous reluctance (SyR) machine test-bench.

Current vector control is used where the dq current references are fetched from the MTPA lookup tables (LUTs); the findings in this paper also applies to other control schemes. Finally, Section V concludes the paper. The analysis puts in evidence the different areas of instability of popular approaches such as the fundamental saliency, the flux cross-product and the active-flux based position observers, as confirmed by the experiments.

II. Sensorless Control System

The electrical rotor position is θ and the electrical angular speed is $\omega = s\,\theta$ where s is the differential operator $\frac{\mathrm{d}}{\mathrm{d}t}$. Estimated vectors are represented by the superscript $\hat{}$. The orthogonal rotational matrix is $\mathbf{J} = \left[\begin{smallmatrix} 0 & -1 \\ 1 & 0 \end{smallmatrix}\right]$ and $\mathbf{I}$ is the identity matrix.

The machine model is expressed in coordinates of estimated rotor reference frame, denoted by subscript $\hat{d}\hat{q}$, whose $\hat{d}$-axis is at $\hat{\theta} = \theta - \tilde{\theta}$, where $\tilde{\theta}$ is the position error. Real space vectors will be used; for example, the stator current is $\boldsymbol{i}_{\hat{d}\hat{q}} = [i_{\hat{d}}, i_{\hat{q}}]^{\mathrm{T}}$ where $i_{\hat{d}}$ and $i_{\hat{q}}$ are the vector components in the estimated rotor reference frame. Space vectors in the stationary reference frame are denoted by subscript $\alpha\beta$. Note that the convention of a SyR machine is followed, i.e, d-axis is defined along the maximum inductance path. This is dictated by the fact that the experimental validation refers to a SyR machine, but all conclusions would be valid also with the d-axis conventionally aligned to PM flux linkage direction.

A. Mathematical Model of a Synchronous Machine

The voltage equation of a synchronous machine in the estimated rotor reference frame is given by

$$s\,\boldsymbol{\lambda}_{\hat{d}\hat{q}} = \boldsymbol{v}_{\hat{d}\hat{q}} - R_s \boldsymbol{i}_{\hat{d}\hat{q}} - \hat{\omega}\,\mathbf{J}\,\boldsymbol{\lambda}_{\hat{d}\hat{q}} \tag{1}$$

where R_s is the stator resistance and $\boldsymbol{\lambda}_{\hat{d}\hat{q}}$ is the stator flux linkage. The synchronous machine exhibits nonlinear magnetic characteristics due to both saturation and cross-saturation phenomenon. Let $\boldsymbol{\Lambda}_{dq}(\boldsymbol{i}_{dq})$ denote the accurate flux-map LUTs of the synchronous machine, shown in Fig. 2. Then, the stator flux in the estimated reference frame can be expressed in terms of the flux-map LUTs as

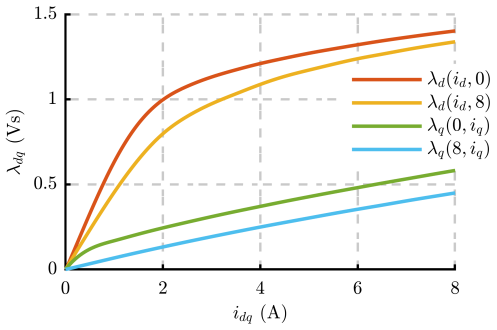

Fig. 2. Flux map of the SyR motor under test exhibiting saturation and cross-saturation characteristics. Experimentally identified with the constant speed test, reported in [26].

$$\boldsymbol{\lambda}_{\hat{d}\hat{q}} = \mathrm{e}^{\mathbf{J}\tilde{\theta}}\,\boldsymbol{\Lambda}_{dq}(\mathrm{e}^{-\mathbf{J}\tilde{\theta}}\boldsymbol{i}_{\hat{d}\hat{q}}). \tag{2}$$

Equivalently, the nonlinear stator flux linkage can be expressed as an operating point dependent linear magnetic model as

$$\boldsymbol{\lambda}_{\hat{d}\hat{q}} = \mathrm{e}^{\mathbf{J}\tilde{\theta}}\,\boldsymbol{L}(\boldsymbol{i}_{dq})\,\mathrm{e}^{-\mathbf{J}\tilde{\theta}}\,\boldsymbol{i}_{\hat{d}\hat{q}} + \mathrm{e}^{\mathbf{J}\tilde{\theta}}\,\boldsymbol{\lambda}_m \tag{3}$$

where the apparent inductance matrix $\boldsymbol{L}$ is a function of the operating point $\boldsymbol{i}_{dq}$ in the real dq rotor reference frame and $\boldsymbol{\lambda_m}$ is the open circuit permanent-magnet flux vector. They are given by

$$\boldsymbol{L}(\boldsymbol{i}_{dq}) = \begin{bmatrix} L_d & 0 \\ 0 & L_q \end{bmatrix} \quad \boldsymbol{\lambda}_m = \begin{bmatrix} 0 \\ -\lambda_m \end{bmatrix} \tag{4}$$

where λ_m is the open circuit permanent-magnet flux linkage and L_d, L_q are the apparent inductances along d and q-axis, respectively. The electromagnetic torque is given by

$$T = \frac{3p}{2}\,\boldsymbol{i}_{\hat{d}\hat{q}}^{\mathrm{T}}\,\mathbf{J}\,\boldsymbol{\lambda}_{\hat{d}\hat{q}} \tag{5}$$

where p is the number of pole pairs.

B. Hybrid Flux Observer

Prior to the state equation of the flux observer, it is useful to introduce the current-model based flux estimation.

1) Current-Model Flux Estimate: The current-model flux linkage based on the flux-map LUTs, denoted with a superscript i, in the estimated rotor reference frame is given by

$$\boldsymbol{\lambda}^{i}_{\hat{d}\hat{q}} = \boldsymbol{\Lambda}_{dq}(\boldsymbol{i}_{\hat{d}\hat{q}}) = \boldsymbol{L}^{i}(\boldsymbol{i}_{\hat{d}\hat{q}}) \cdot \boldsymbol{i}_{\hat{d}\hat{q}} + \boldsymbol{\lambda}_m \tag{6}$$

where $\boldsymbol{L}^i$ is the current-model apparent inductance matrix that is a function of the operating point $\boldsymbol{i}_{\hat{d}\hat{q}}$ in the estimated $\hat{d}\hat{q}$ reference frame. The veracity of the current-model flux is dependent on the position error, i.e., for synchronous machines with saturation, only in the absence of position error does the equalities $\boldsymbol{\lambda}_{dq} = \boldsymbol{\lambda}^{i}_{dq}$ and $\boldsymbol{L} = \boldsymbol{L}^{i}$ hold.

2) State Equation: The hybrid flux observer is a combination of the back-emf integral (voltage-model) and the current-model fluxes, defined in the stationary reference frame as

$$s\hat{\boldsymbol{\lambda}}_{\alpha\beta} = \boldsymbol{v}_{\alpha\beta} - R_s \boldsymbol{i}_{\alpha\beta} + \mathrm{e}^{\mathbf{J}\hat{\theta}}\, \boldsymbol{G}\left(\boldsymbol{\lambda}^{i}_{\hat{d}q} - \hat{\boldsymbol{\lambda}}_{\hat{d}q}\right) \tag{7}$$

where $\boldsymbol{G}$ is a 2×2 gain matrix. Accurate parameter estimate of stator resistance is assumed. In the estimated rotor reference frame, (7) transforms to

$$s\,\hat{\boldsymbol{\lambda}}_{\hat{d}q} = \boldsymbol{v}_{\hat{d}q} - R_s \boldsymbol{i}_{\hat{d}q} - \hat{\omega}\mathbf{J}\,\hat{\boldsymbol{\lambda}}_{\hat{d}q} + \boldsymbol{G}\left(\boldsymbol{\lambda}^{i}_{\hat{d}q} - \hat{\boldsymbol{\lambda}}_{\hat{d}q}\right) \tag{8}$$

To aid in further analysis, the nonlinear flux estimation error dynamics is derived from (1) and (8) as

$$s\,\tilde{\boldsymbol{\lambda}}_{\hat{d}q} = -(\boldsymbol{G} + \hat{\omega}\mathbf{J})\,\tilde{\boldsymbol{\lambda}}_{\hat{d}q} + \boldsymbol{G}\,(\boldsymbol{\lambda}_{\hat{d}q} - \boldsymbol{\lambda}^{i}_{\hat{d}q}) \tag{9}$$

where $\tilde{\boldsymbol{\lambda}}_{\hat{d}q} = \boldsymbol{\lambda}_{\hat{d}q} - \hat{\boldsymbol{\lambda}}_{\hat{d}q}$ is the flux estimation error. The relationship between the real stator flux $\boldsymbol{\lambda}_{\hat{d}q}$ and the current model estimate $\boldsymbol{\lambda}^{i}_{\hat{d}q}$ in the estimated reference frame is established in the following section.

C. Magnetic Model Accounting Position Error (MMAP)

Linearizing the stator flux linkage (2) around an operating point gives

$$\boldsymbol{\lambda}_{\hat{d}q} = \left(\mathbf{I} + \tilde{\theta}\,\mathbf{J}\right)\left(\boldsymbol{\Lambda}_{dq}(\boldsymbol{i}_{\hat{d}q}) - \tilde{\theta}\,\frac{\partial \boldsymbol{\Lambda}_{dq}}{\partial \boldsymbol{i}_{\hat{d}q}}\,\mathbf{J}\,\boldsymbol{i}_{\hat{d}q}\right) \tag{10}$$

The time derivative of stator flux can be expressed with the incremental inductance matrix $\boldsymbol{L}_{\partial}$ as

$$\frac{\partial \boldsymbol{\lambda}_{dq}}{\partial \boldsymbol{i}_{dq}} = \boldsymbol{L}_{\partial}(\boldsymbol{i}_{dq}) = \begin{bmatrix} l_d & l_{dq} \\ l_{dq} & l_q \end{bmatrix} \tag{11}$$

where l_d, l_q represents the incremental inductance along direct d and quadrature q axis, respectively, while l_{dq} is the cross-saturation term.

The first order approximation holds for small position error, i.e., a constant incremental inductance in the vicinity of the operating point is assumed. Simplifying (10), the magnetic model accounting position error (MMAP) is derived as

$$\boldsymbol{\lambda}_{\hat{d}q} = \boldsymbol{\lambda}^{i}_{\hat{d}q} + \tilde{\theta}\,\boldsymbol{\lambda}^{a}_{\hat{d}q} \tag{12}$$

where the auxiliary-flux vector $\boldsymbol{\lambda}^{a}_{\hat{d}q}$ for nonlinear magnetic model is given by

$$\boldsymbol{\lambda}^{a}_{\hat{d}q} = \mathbf{J}\,\boldsymbol{\lambda}^{i}_{\hat{d}q} - \boldsymbol{L}_{\partial}\,\mathbf{J}\,\boldsymbol{i}_{\hat{d}q}. \tag{13}$$

Using MMAP (12) in (9), the linearized flux estimation error dynamics as a function of position error is given by

$$\tilde{\boldsymbol{\lambda}}_{\hat{d}q} = (s\mathbf{I} + \boldsymbol{G} + \omega\mathbf{J})^{-1}\,\boldsymbol{G}\,\boldsymbol{\lambda}^{a}_{\hat{d}q}\,\tilde{\theta}. \tag{14}$$

This will be used in the following section to formulate the position error signal.

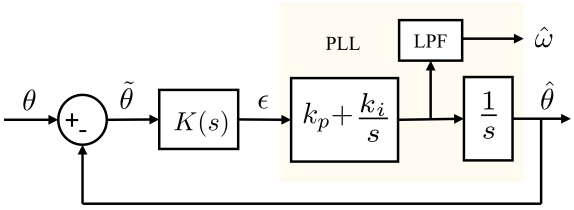

Fig. 3. Closed loop analysis of the position observer with PLL

III. Projection Vector Framework

A. Definition

The position error signal ϵ driving the observer adaptation law is expressed in a general form as the projection of difference in the observed and the current-model flux estimates on a projection vector $\boldsymbol{\phi}$ as [14] [16]

$$\epsilon = \boldsymbol{\phi}^{\mathrm{T}}\,(\hat{\boldsymbol{\lambda}}_{\hat{d}q} - \boldsymbol{\lambda}^{i}_{\hat{d}q}) \tag{15}$$

Using flux estimation error $\tilde{\boldsymbol{\lambda}}_{\hat{d}q} = \boldsymbol{\lambda}_{\hat{d}q} - \hat{\boldsymbol{\lambda}}_{\hat{d}q}$ and MMAP (12), the linearized form of (15) becomes

$$\epsilon = \boldsymbol{\phi}^{\mathrm{T}}\left(\boldsymbol{\lambda}^{a}_{\hat{d}q}\,\tilde{\theta} - \tilde{\boldsymbol{\lambda}}_{\hat{d}q}\right) \tag{16}$$

Following the results of flux estimation error dynamics (14), the transfer function between the error signal and the position error is derived as

$$K(s) = \frac{\epsilon}{\tilde{\theta}} = \boldsymbol{\phi}^{\mathrm{T}}\,(s\mathbf{I} + \boldsymbol{G} + \omega\mathbf{J})^{-1}(s\mathbf{I} + \omega\mathbf{J})\,\boldsymbol{\lambda}^{a}_{\hat{d}q}. \tag{17}$$

The transfer function K is depicted in the block diagram of the closed-loop position observer in Fig. 3.

B. Speed and Position Observer

A conventional phase-locked-loop (PLL) with a proportional-integral (PI) controller is employed to drive the position error signal ϵ to zero as

$$\hat{\omega} = k_p\,\epsilon + \omega_i \qquad \omega_i = \int k_i\,\epsilon\,\mathrm{d}t \qquad \hat{\theta} = \int \hat{\omega}\,\mathrm{d}t \tag{18}$$

where k_p and k_i are the respective gains. The gains of the PLL are tuned for a critically damped response considering $\epsilon = \tilde{\theta}$ at $s = -\Omega_\omega$ ($k_p = 2\,\Omega_\omega$ & $k_i = \Omega_\omega^2$).

C. Stability Analysis

The system stability analysis comprising of flux and position observers is designed for a general projection vector. To this end, the error dynamics of the position observer in (18) can be expressed as

$$s\,\tilde{\theta} = \tilde{\omega}_i - k_p\,\epsilon \qquad s\,\tilde{\omega}_i = -k_i\,\epsilon. \tag{19}$$

The combined dynamics of the flux and the position observers is given by

$$s\,\boldsymbol{y} = \boldsymbol{A}\,\boldsymbol{y} \tag{20}$$

$$\boldsymbol{A} = \begin{bmatrix} -(\boldsymbol{G} + \omega\,\mathbf{J}) & \boldsymbol{G}\,\boldsymbol{\lambda}^{a}_{\hat{d}q} & \mathbf{0} \\ k_p\,\boldsymbol{\phi}^{\mathrm{T}} & -k_p\,\boldsymbol{\phi}^{\mathrm{T}}\boldsymbol{\lambda}^{a}_{\hat{d}q} & 1 \\ k_i\,\boldsymbol{\phi}^{\mathrm{T}} & -k_i\,\boldsymbol{\phi}^{\mathrm{T}}\boldsymbol{\lambda}^{a}_{\hat{d}q} & 0 \end{bmatrix}$$

TABLE I
MOTOR PARAMETERS

Parameters	Symbol	Values	Units
Rated power	P_n	1.1	kW
Rated voltage	V_n	340	V
Rated speed	ω_n	1500	rpm
Rated current	I_n	2.3	A
Rated torque	T_n	7.1	Nm
Pole pairs	p	2	-
Stator resistance	R_s	6.8	Ω
Shaft inertia	J	0.04	kgm^2

where $\boldsymbol{y} = \left[\left(\tilde{\boldsymbol{\lambda}}_{\hat{dq}}\right)^{\mathrm{T}} \quad \tilde{\theta} \quad \tilde{\omega}_i\right]^{\mathrm{T}}$. The eigenvalues of (20) are computed for each operating point to evaluate the system stability.

D. Experimental Setup

The stability analysis of the sensorless techniques is validated experimentally with a 1.1 kW SyR motor test-bench on a dSPACE DS1103 control platform running at a sampling frequency of 10 kHz. The parameters of the SyR motor under test are tabulated in Table I.

The SyR machine operates in the speed control mode where the load torque is imposed by an auxiliary drive. A minimum stator current $i_{min} = 1$ A (0.25 p.u.) is set for fundamental excitation at no load. Unless otherwise mentioned, the flux observer gain $\boldsymbol{G} = g\,\mathbf{I}$ is tuned as $g = 2\pi \cdot 10$ rad/s and the PLL gains are tuned for critical damping at $\Omega_\omega = 2\pi \cdot 50$ rad/s.

The incremental inductance matrix $\boldsymbol{L}_\partial$ is retrieved in real-time from the flux-map; as an example:

$$l_d(\boldsymbol{i}_{dq}) = \frac{\boldsymbol{\Lambda}_d(i_d + \delta i_d, i_q) - \boldsymbol{\Lambda}_d(i_d, i_q)}{\delta i_d} \tag{21}$$

where δi_d is a small value (≈ 10 mA). The other incremental inductances are computed in a similar fashion.

IV. FLUX OBSERVER-BASED SENSORLESS TECHNIQUES

Six fundamental-wave excitation techniques based on the flux observer from literature are discussed through the common prism of projection vector framework. The regions of instability and operational limits for each technique are identified. The sensitivity analysis to parameter errors is reported in [15]; accurate parameter are considered in this work.

A. Flux Cross-Product Position Observer (CP)

1) Projection Vector Definition: The discrepancy in the phase angle between the observed and the current-model flux estimates is exploited for position tracking. In [5]–[7], the sine and cosine of the rotor position are estimated directly as

$$\sin(\hat{\theta}) = \frac{\lambda^i_{\hat{d}}\,\hat{\lambda}_\beta - \lambda^i_{\hat{q}}\,\hat{\lambda}_\alpha}{|\boldsymbol{\lambda}^i_{\hat{dq}}|^2} \qquad \cos(\hat{\theta}) = \frac{\lambda^i_{\hat{d}}\,\hat{\lambda}_\alpha + \lambda^i_{\hat{q}}\,\hat{\lambda}_\beta}{|\boldsymbol{\lambda}^i_{\hat{dq}}|^2}. \tag{22}$$

To access the compatibility of this technique with a PLL, the position error signal ϵ_{cp} is derived from the cross-product

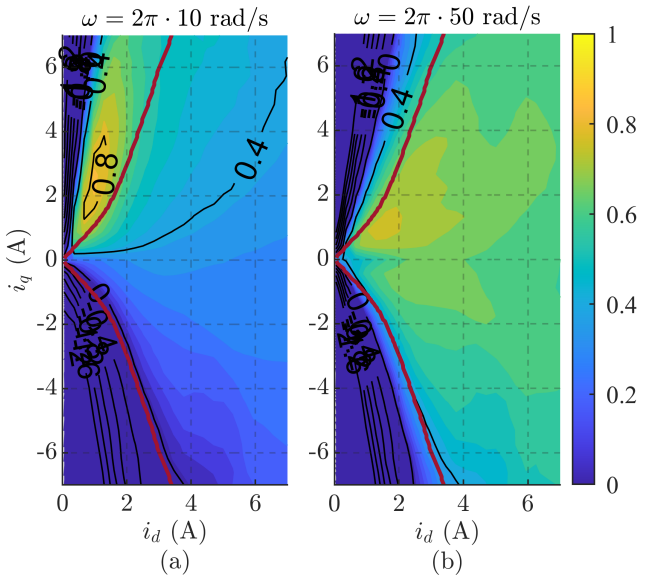

Fig. 4. The contour plot of the transfer function (26) for the CP position observer: (a) $\omega = 2\pi \cdot 10$ rad/s (0.2 p.u.); (b) $\omega = 2\pi \cdot 50$ rad/s (1 p.u.). Flux observer gain is $g = 2\pi \cdot 10$ rad/s. The red line is the MTPA trajectory.

of the current-model and the observed flux in the estimated reference frame as

$$\epsilon_{cp} = \frac{\lambda^i_{\hat{d}}\,\hat{\lambda}_{\hat{q}} - \lambda^i_{\hat{q}}\,\hat{\lambda}_{\hat{d}}}{|\boldsymbol{\lambda}^i_{\hat{dq}}|^2} = \frac{-1}{|\boldsymbol{\lambda}^i_{\hat{dq}}|^2}\left(\boldsymbol{\lambda}^i_{\hat{dq}}\right)^{\mathrm{T}} \mathbf{J}\,\hat{\boldsymbol{\lambda}}_{\hat{dq}}. \tag{23}$$

This scheme will be denoted by the acronym CP and the subscript *cp*, implying cross-product. The error signal is expressed in the projection vector framework as

$$\epsilon_{cp} = \boldsymbol{\phi}^{\mathrm{T}}_{cp}\left(\hat{\boldsymbol{\lambda}}_{\hat{dq}} - \boldsymbol{\lambda}^i_{\hat{dq}}\right) \tag{24}$$

where the projection vector $\boldsymbol{\phi}_{cp}$ corresponding to the error signal (23) is given by

$$\boldsymbol{\phi}^{\mathrm{T}}_{cp} = \frac{-1}{|\boldsymbol{\lambda}^i_{\hat{dq}}|^2}\left(\boldsymbol{\lambda}^i_{\hat{dq}}\right)^{\mathrm{T}} \mathbf{J}. \tag{25}$$

2) Stability Analysis: For $\boldsymbol{G} = g\,\mathbf{I}$ and using the CP projection vector (25) in (17), the dc-gain of the transfer function between the error signal and the position error becomes

$$K_{cp}\big|_{s=0} = \frac{\omega^2}{g^2 + \omega^2}\,\frac{\left(\boldsymbol{\lambda}^i_{\hat{dq}}\right)^{\mathrm{T}}}{|\boldsymbol{\lambda}^i_{\hat{dq}}|^2}\left[\frac{g}{\omega}\,\boldsymbol{\lambda}^a_{\hat{dq}} - \mathbf{J}\,\boldsymbol{\lambda}^a_{\hat{dq}}\right]. \tag{26}$$

The expression (26) can be loosely interpreted as an open-loop gain, see Fig. 3, i.e., small values indicate poor observability of the position error and poor resilience to parameter errors. A negative value implies a positive feedback and is unstable.

The gain (26) is dependent on the operating point $\boldsymbol{i}_{dq}$ and the angular speed ω. The contour of (26) in the dq current plane for the SyR motor under test is shown in Fig. 4 at low speed (0.2 p.u.) and rated speed. For speeds below 0.2 p.u., typically, a high-frequency excitation based schemes are employed. It can be discerned that the braking regions on the MTPA trajectory are vulnerable, particularly at low speeds.

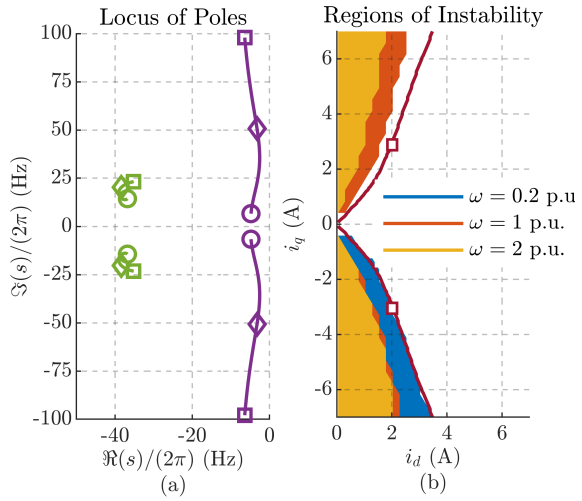

Fig. 5. Closed-loop stability analysis of the CP position observer: (a) Locus of poles of the flux (purple) and the position (green) observer at the rated torque (MTPA). Markers: ○ is 0.1 p.u., ◇ is 1 p.u. and □ is 2 p.u.; (b) Regions of instability at different speeds where the marker □ denotes rated torque.

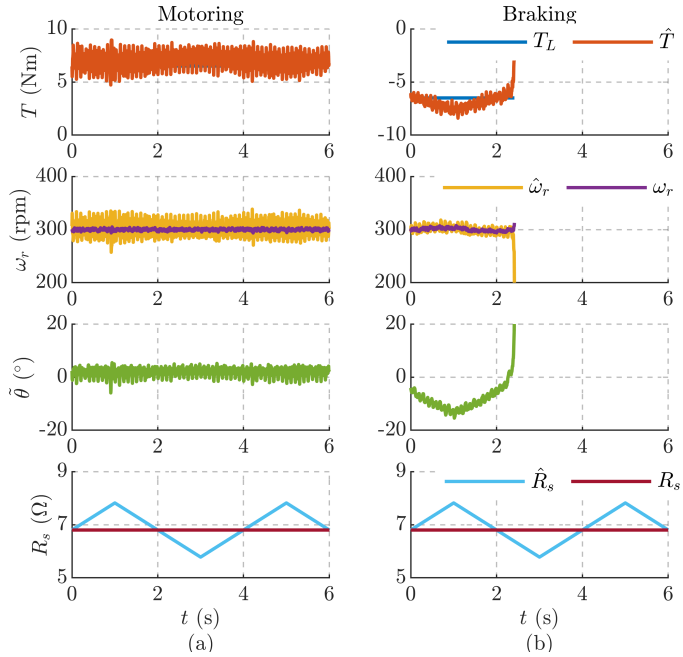

Fig. 6. CP position observer stability analysis with resistance perturbation of ±15% error, $\tilde{R}_s = \pm 0.15\, R_s$ at 300 rpm (0.2 p.u.) and rated torque: (a) Motoring; (b) Braking.

Moreover, high speed operations in flux-weakening region shows poor signal strength and can be potentially unstable.

The locus of poles (20) for the CP projection vector (25) at rated torque (motoring) is shown in Fig. 5(a) and is observed to be stable at all speeds. A comprehensive stability analysis at all operating point in the dq current plane is evaluated and the regions of instability are sketched in Fig. 5(b). Low speeds braking and high speeds flux-weakening regions are identified as critical for stability.

3) Experimental Results: To evaluate the stability of the sensorless techniques, a small perturbation of ± 15% in the control stator resistance is introduced as shown in Fig. 6 at 300 rpm. Figs. 6(a) and 6(b) show the motoring and braking operation at rated torque, respectively.

It can be observed that the motoring operation of the CP observer is stable while the braking runs into instability. The results corroborate the stability analysis in Fig. 5(b) where the rated torque at 300 rpm in braking operation on the MTPA trajectory (denoted by the marker □) is at close proximity to the unstable region.

B. Active-Flux Position Observer (AF)

1) Projection Vector Definition: The active-flux observer is a commonly used technique in literature [8]–[11] for position estimation. By definition, the active-flux is the torque producing component of the stator flux that is inherently along the d-axis, represented in the estimated rotor reference as

$$\boldsymbol{\lambda}^{af}_{\hat{d}\hat{q}} = \boldsymbol{\lambda}_{\hat{d}\hat{q}} - L_q\, \boldsymbol{i}_{\hat{d}\hat{q}}. \tag{27}$$

Using (3) and linearzing leads to

$$\boldsymbol{\lambda}^{af}_{\hat{d}\hat{q}} = \begin{bmatrix} (L_d - L_q)\, i_{\hat{d}} \\ 0 \end{bmatrix} + \tilde{\theta}\, 2\, L_\Delta \begin{bmatrix} i_{\hat{q}} \\ i_{\hat{d}} \end{bmatrix} \tag{28}$$

where $L_\Delta = (L_d - L_q)/2$. The q-axis component $\lambda^{af}_{\hat{q}}$ is proportional to the position error; thus, the error signal can be derived using the observed stator flux ($\boldsymbol{\lambda}_{\hat{d}\hat{q}} \to \hat{\boldsymbol{\lambda}}_{\hat{d}\hat{q}}$) and the current-model inductance ($\boldsymbol{L} \to \boldsymbol{L}^i$) in (28) as

$$\epsilon_{af} = \frac{1}{2\, L^i_\Delta\, i_{\hat{d}}} \begin{bmatrix} 0 \\ 1 \end{bmatrix}^{\mathrm{T}} \left(\hat{\boldsymbol{\lambda}}_{\hat{d}\hat{q}} - L^i_q\, \boldsymbol{i}_{\hat{d}\hat{q}} \right). \tag{29}$$

This scheme is denoted by the acronym AF and the subscript af. The equivalent projection vector for the error signal (29) of the active-flux position observer is

$$\boldsymbol{\phi}^{\mathrm{T}}_{af} = \frac{1}{2\, L^i_\Delta\, i_{\hat{d}}} \begin{bmatrix} 0 \\ 1 \end{bmatrix}^{\mathrm{T}}. \tag{30}$$

2) Stability Analysis: Using $\boldsymbol{G} = g\,\mathbf{I}$, the dc-gain of the transfer function (17) for the AF projection vector (30) is given by

$$K_{af}\big|_{s=0} = \frac{\omega^2}{g^2 + \omega^2}\, \frac{1}{2\, L_\Delta\, i_{\hat{d}}} \left[\frac{g}{\omega}\, \lambda^a_{\hat{d}} + \lambda^a_{\hat{q}} \right]. \tag{31}$$

The gain (31) is dependent on the operating point $\boldsymbol{i}_{dq}$ and the angular speed ω. The contour plot is shown in Fig. 7 at two different speeds where the braking region is observed to have poor signal strength that deteriorates with decreasing speed.

The locus of poles at the rated torque (motoring) is shown in Fig. 8(a) which is stable at all speeds. A comprehensive evaluation for stability in the dq current plane at three different speeds is shown in Fig. 8(b). As mentioned earlier, the low speed braking regions is susceptible. It is interesting to point out that unstable regions exist also at high speeds motoring despite a healthy signal strength in Fig. 7; this arises due to the dynamic coupling between flux and position observer [16].

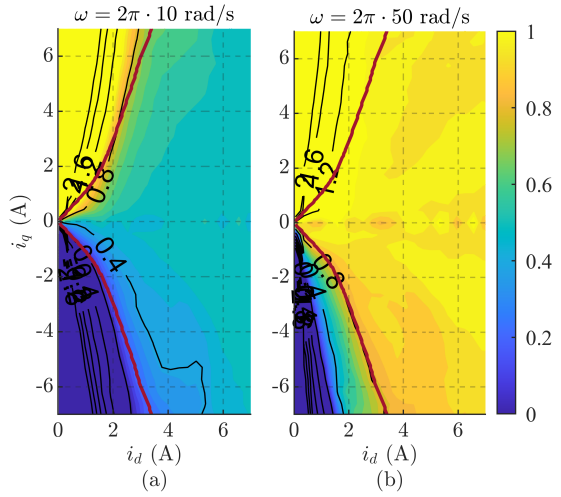

Fig. 7. The contour plot of the transfer function (31) for the AF position observer: (a) $\omega = 2\pi \cdot 10$ rad/s (0.2 p.u.); (b) $\omega = 2\pi \cdot 50$ rad/s (1 p.u.). Flux observer gain is $g = 2\pi \cdot 10$ rad/s. The red line is the MTPA trajectory.

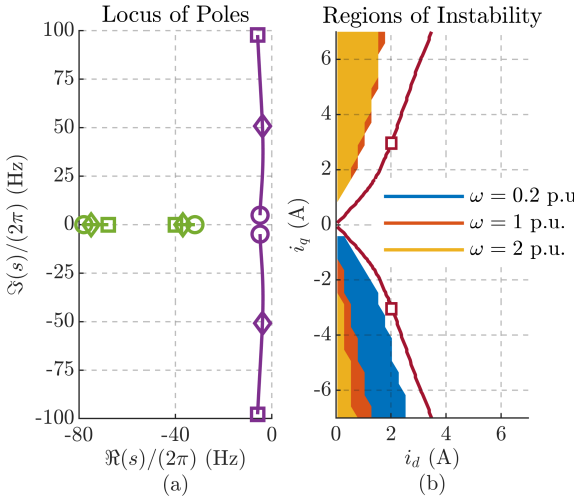

Fig. 8. Closed-loop stability analysis of the AF position observer: (a) Locus of poles of the flux (purple) and the position (green) observer at the rated torque (MTPA). Markers: ○ is 0.1 p.u., ◇ is 1 p.u. and □ is 2 p.u.; (b) Regions of instability at different speeds where the marker □ denotes the rated torque.

3) Experimental Results: Figs. 9(a) and 9(b) show the experimental validation of the stability of AF position observer with a control resistance perturbation in motoring and braking operation, respectively.

The motoring at rated torque and 300 rpm is stable while the braking becomes unstable. This corroborates the stability analysis in Fig. 8(b) where the rated torque in braking (denoted by the marker □) is near the unstable region at operating speed of 0.2 p.u.

C. Fundamental Saliency-based Position Observer (FS)

1) Projection Vector Definition: This technique aims to estimate the rotor position from the anisotropic component of the stator flux. Developed for a SyR machine in [12], it is extended for a general synchronous machines. To this end,

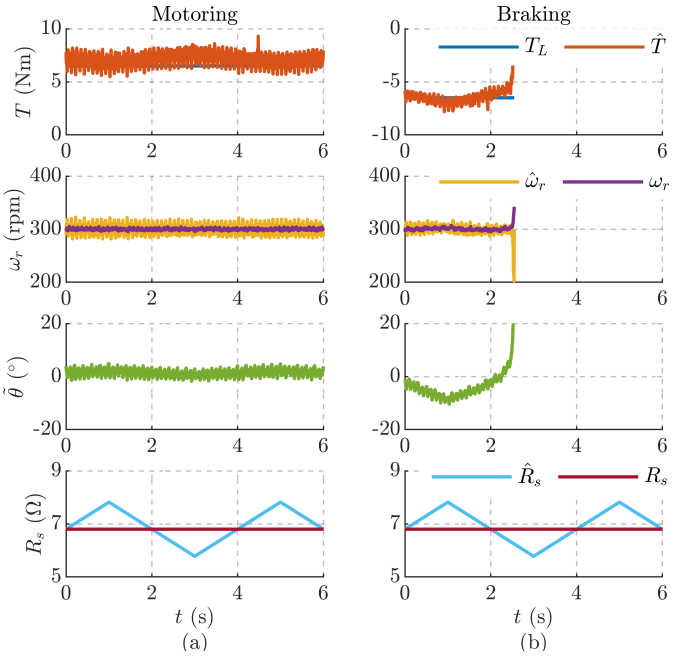

Fig. 9. AF position observer stability analysis with resistance perturbation of ±15% error, $\tilde{R}_s = \pm 0.15\, R_s$ at 300 rpm (0.2 p.u.) and rated torque: (a) Motoring; (b) Braking.

decomposing the stator flux in the estimated rotor reference frame (3) to isotropic and anisotropic terms leads to

$$\boldsymbol{\lambda}_{\hat{dq}} = L_\Sigma\, \boldsymbol{i}_{\hat{dq}} + L_\Delta\, \mathrm{e}^{2\mathbf{J}\,\tilde{\theta}}\, \bar{\boldsymbol{i}}_{\hat{dq}} + \mathrm{e}^{\mathbf{J}\tilde{\theta}}\, \boldsymbol{\lambda}_m \tag{32}$$

where $L_\Sigma = \frac{L_d + L_q}{2}$ and $\bar{\boldsymbol{i}}_{\hat{dq}} = \begin{bmatrix} i_{\hat{d}} & -i_{\hat{q}} \end{bmatrix}^{\mathrm{T}}$ is the conjugate vector. Linearizing (32), the position error can be extracted as

$$\tilde{\theta} = \frac{\left(\mathbf{J}\,\boldsymbol{\lambda}_{\hat{dq}} - \boldsymbol{L}\,\mathbf{J}\,\boldsymbol{i}_{\hat{dq}}\right)^{\mathrm{T}}}{|\mathbf{J}\,\boldsymbol{\lambda}_{\hat{dq}} - \boldsymbol{L}\,\mathbf{J}\,\boldsymbol{i}_{\hat{dq}}|^2} \left(\boldsymbol{\lambda}_{\hat{dq}} - \boldsymbol{L}\,\boldsymbol{i}_{\hat{dq}} - \boldsymbol{\lambda}_m\right). \tag{33}$$

This scheme is denoted by the acronym FS and the subscript fs. To design the position error function following (33), the real stator flux is replaced by the observed flux ($\boldsymbol{\lambda}_{\hat{dq}} \to \hat{\boldsymbol{\lambda}}_{\hat{dq}}$) and the real inductance is replaced by the current-model inductance ($\boldsymbol{L} \to \boldsymbol{L}^i$) as

$$\epsilon_{fs} = \boldsymbol{\phi}_{fs}^{\mathrm{T}}\, (\hat{\boldsymbol{\lambda}}_{\hat{dq}} - \boldsymbol{\lambda}^i_{\hat{dq}}) \tag{34}$$

where the FS projection vector is given by

$$\boldsymbol{\phi}_{fs}^{\mathrm{T}} = \frac{\left(\mathbf{J}\,\boldsymbol{\lambda}^i_{\hat{dq}} - \boldsymbol{L}^i\,\mathbf{J}\,\boldsymbol{i}_{\hat{dq}}\right)^{\mathrm{T}}}{|\mathbf{J}\,\boldsymbol{\lambda}^i_{\hat{dq}} - \boldsymbol{L}^i\,\mathbf{J}\,\boldsymbol{i}_{\hat{dq}}|^2}. \tag{35}$$

It is worth pointing out that the FS projection vector is along the auxiliary-flux (13) at linear unsaturated regions, i.e., incremental inductance equal to the apparent inductance.

2) Stability Analysis: The dc-gain of the transfer function (17) with $\boldsymbol{G} = g\,\mathbf{I}$ for the FS projection vector (35) becomes

$$K_{fs}\big|_{s=0} = \frac{\omega^2}{g^2 + \omega^2} \frac{\left(\mathbf{J}\,\boldsymbol{\lambda}^i_{\hat{dq}} - \boldsymbol{L}^i\,\mathbf{J}\,\boldsymbol{i}_{\hat{dq}}\right)^{\mathrm{T}}}{|\mathbf{J}\,\boldsymbol{\lambda}^i_{\hat{dq}} - \boldsymbol{L}^i\,\mathbf{J}\,\boldsymbol{i}_{\hat{dq}}|^2} \left[\frac{g}{\omega}\,\mathbf{J}\,\boldsymbol{\lambda}^a_{\hat{dq}} + \boldsymbol{\lambda}^a_{\hat{dq}}\right]. \tag{36}$$

The gain (36) is dependent on the operating point $\boldsymbol{i}_{dq}$ and the angular speed ω. The contour in the dq current plane is shown

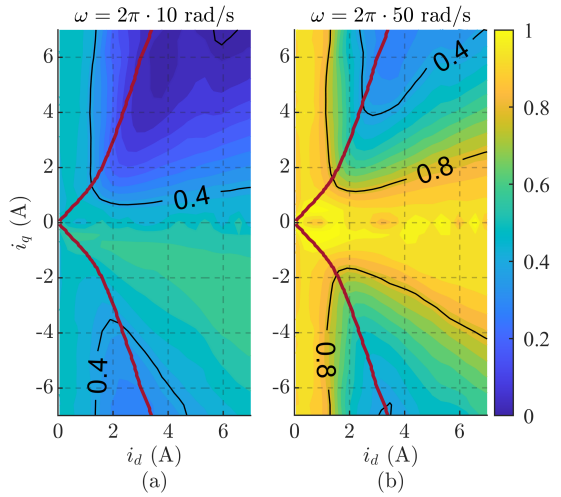

Fig. 10. The contour plot of the transfer function (36) for the FS position observer: (a) $\omega = 2\pi \cdot 10$ rad/s (0.2 p.u.); (b) $\omega = 2\pi \cdot 50$ rad/s (1 p.u.). Flux observer gain is $g = 2\pi \cdot 10$ rad/s. The red line is the MTPA trajectory.

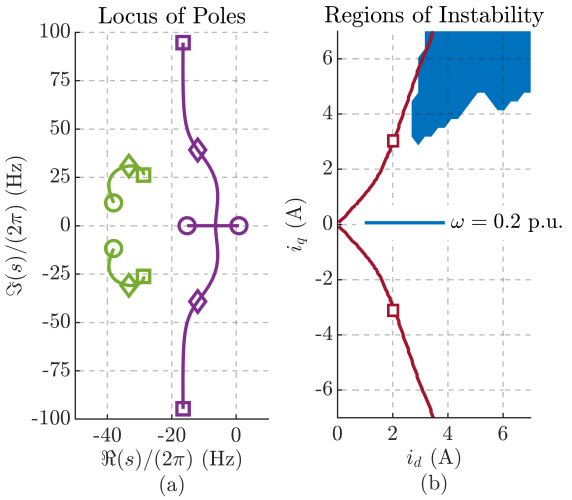

Fig. 11. Closed-loop stability analysis of the FS position observer: (a) Locus of poles of the flux (purple) and the position (green) observer at the rated torque (MTPA). Markers: ○ is 0.1 p.u., ◇ is 1 p.u. and □ is 2 p.u.; (b) Regions of instability where the marker □ denotes the rated torque.

in Fig. 10 at two different speeds; the motoring operation at the low speeds region has a poor signal strength and is vulnerable to instability under parameter errors.

The locus of closed-loop poles (20) at the rated torque (motoring) is shown in Fig. 11(a) where the poles are seen moving towards the positive plane at low speeds. The regions of instability at low speed (0.2 p.u.) are mapped in the dq current plane in Fig. 11(b); the motoring operation at high load is susceptible which is coherent with the poor signal quality in Fig. 10. No unstable regions were identified at medium and high speeds.

3) Experimental Results: The stability analysis is validated with the control resistance perturbation at rated torque and 300 rpm in motoring and braking operation as shown in Figs. 12(a) and 12(b), respectively.

The motoring operation is observed to be unstable while the

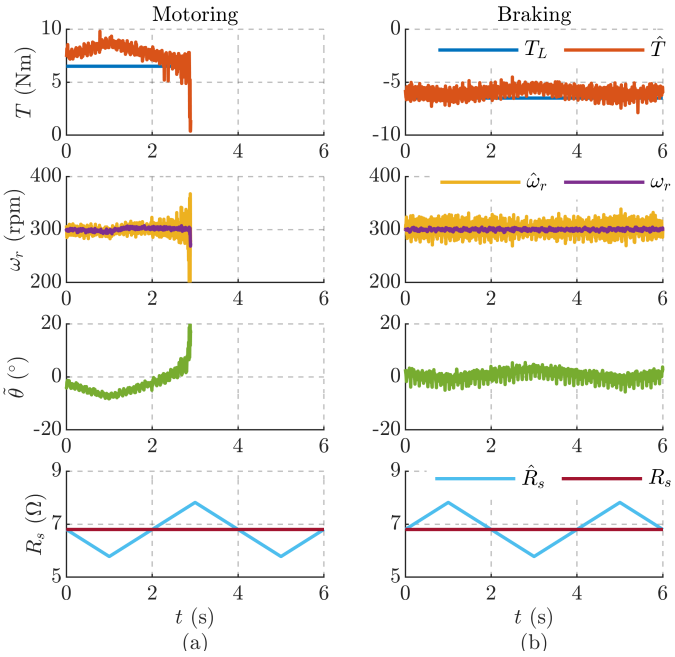

Fig. 12. FS position observer stability analysis with resistance perturbation of ±15% error, $\tilde{R}_s = \pm 0.15\, R_s$ at 300 rpm (0.2 p.u.) and rated torque: (a) Motoring; (b) Braking.

braking is stable. This corroborates with the stability analysis in Fig. 11(b) where the rated torque in motoring (denoted by the marker □) is at close proximity to the instability region at 300 rpm.

D. Auxiliary-Flux Position Observer (AUX)

1) Projection Vector Definition: To mitigate the instability problems of active-flux method while retaining the simplicity, an auxiliary-flux position observer is proposed in [13]. The auxiliary-flux defined in (13) is the discrepancy between the voltage and current-model flux estimates scaled by the position error, i.e.,

$$\tilde{\theta} = \frac{\left(\boldsymbol{\lambda}^a_{\hat{d}\hat{q}}\right)^{\mathrm{T}}}{|\boldsymbol{\lambda}^a_{\hat{d}\hat{q}}|^2}\left(\boldsymbol{\lambda}_{\hat{d}\hat{q}} - \boldsymbol{\lambda}^i_{\hat{d}\hat{q}}\right) \tag{37}$$

Hence, using the observed stator flux ($\boldsymbol{\lambda}_{\hat{d}\hat{q}} \to \hat{\boldsymbol{\lambda}}_{\hat{d}\hat{q}}$), a natural choice for error signal is along the auxiliary-flux vector as

$$\epsilon_{aux} = \boldsymbol{\phi}^{\mathrm{T}}_{aux}\left(\hat{\boldsymbol{\lambda}}_{\hat{d}\hat{q}} - \boldsymbol{\lambda}^i_{\hat{d}\hat{q}}\right) \tag{38}$$

where the auxiliary-flux projection vector is given by

$$\boldsymbol{\phi}^{\mathrm{T}}_{aux} = \frac{\left(\boldsymbol{\lambda}^a_{\hat{d}\hat{q}}\right)^{\mathrm{T}}}{|\boldsymbol{\lambda}^a_{\hat{d}\hat{q}}|^2}. \tag{39}$$

This scheme is denoted by the acronym AUX and the subscript aux.

2) Stability Analysis: The dc-gain of the transfer function (17) with $\boldsymbol{G} = g\,\mathbf{I}$ for AUX projection vector (39) is given by

$$K_{aux}\big|_{s=0} = \frac{\omega^2}{g^2 + \omega^2} \tag{40}$$

Differing from the former three schemes, the gain (40) is only dependent on the square of angular speed ω and not the

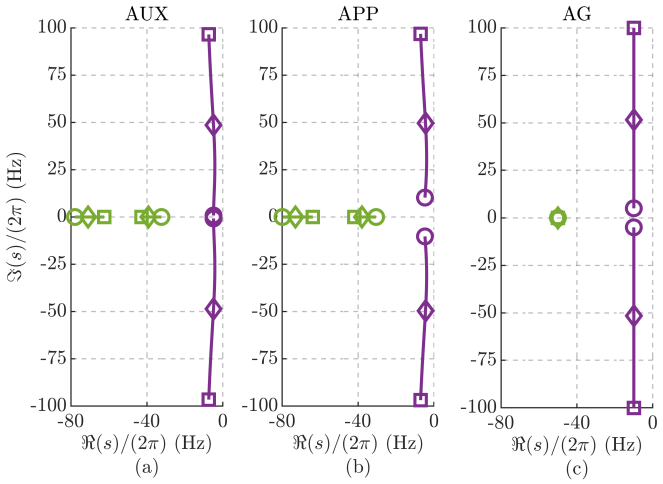

Fig. 13. Locus of poles of the flux (purple) and the position (green) observer: (a) AUX position observer; (b) APP position observer; (c) AG position observer. Markers: ○ is 0.1 p.u., ◇ is 1 p.u. and □ is 2 p.u.

operating point $\boldsymbol{i}_{dq}$. Hence, a sufficient strength of the signal is ensured, with minimum of 0.5 at the low speed $\omega = g$ and progressively increasing at higher speeds.

The locus of the closed-loop poles (20) is a function of angular speed and independent of operating torque. The poles are stable at all speeds as shown in Fig. 13(a).

3) Experimental Results: The performance of the AUX position observer under control resistance perturbation at rated torque and 300 rpm in motoring and braking operation is shown in Figs. 14(a) and 14(b), respectively. The control is stable as ascertained in the former analysis. The position error and the estimated torque are observed to be susceptible to the resistance perturbations.

E. APP Position Observer (APP)

1) Projection Vector Definition and Stability Analysis: The APP projection vector is designed from the linearized error dynamics of the flux observer such that the dc-gain of the transfer function (17) is unity, i.e.,

$$K_{app}|_{s=0} = 1. \tag{41}$$

This leads to a projection vector of nature:

$$\boldsymbol{\phi}_{app}^{\mathrm{T}} = \frac{-1}{\omega\,|\boldsymbol{\lambda}_{\hat{dq}}^{a}|^2}\,\left(\boldsymbol{\lambda}_{\hat{dq}}^{a}\right)^{\mathrm{T}}\mathbf{J}\left(\boldsymbol{G} + \omega\,\mathbf{J}\right) \tag{42}$$

This scheme is denoted by the acronym APP and the subscript app. This choice of projection vector has an unique advantage of immunity from the voltage errors due to stator resistance variation and non-ideal inverter compensation [15].

The locus of the closed-loop poles at different speeds is shown in Fig. 13(b) and is observed to be stable at all operating regions. The poles, however, differ from the designated value due to dynamic coupling between the flux and the position observer.

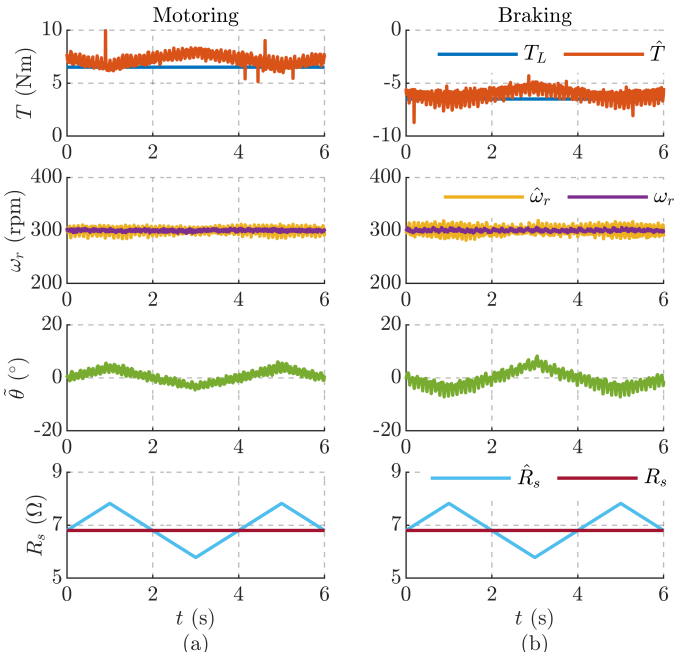

Fig. 14. AUX position observer stability analysis with resistance perturbation of ±15% error, $\tilde{R}_s = \pm 0.15\,R_s$ at 300 rpm (0.2 p.u.) and rated torque: (a) Motoring; (b) Braking.

2) Experimental Results: The experimental validation of the APP position observer with control resistance perturbations at rated torque and 300 rpm is shown in Fig. 15. In addition to the stability, it can be discerned that the position error remains unperturbed despite the resistance variations, demonstrating the resistance immunity property of the APP scheme [15].

F. Adaptive-Gain Position Observer (AG)

1) Projection Vector Definition and Stability Analysis: Denoted by the acronym AG and the subscript ag, the adaptive-gain approach proposed in [16] aims to decouple the dynamics of flux and position observer, i.e.,

$$K_{ag}(s) = 1 \tag{43}$$

To this end, the transfer function (17) can be manipulated to

$$K_{ag}(s) = \boldsymbol{\phi}_{ag}^{\mathrm{T}}\,\boldsymbol{\lambda}_{\hat{dq}}^{a} - \boldsymbol{\phi}_{ag}^{\mathrm{T}}\left(s\mathbf{I} + \boldsymbol{G} + \omega\mathbf{J}\right)^{-1}\boldsymbol{G}\,\boldsymbol{\lambda}_{\hat{dq}}^{a}. \tag{44}$$

The gain $\boldsymbol{G}$ is adapted such that $\boldsymbol{G}\,\boldsymbol{\lambda}_{\hat{dq}}^{a} = 0$. Then, it follows that a projection vector along the auxiliary-flux vector satisfies the condition (43) as

$$\boldsymbol{\phi}_{ag}^{\mathrm{T}} = \frac{\left(\boldsymbol{\lambda}_{\hat{dq}}^{a}\right)^{\mathrm{T}}}{|\boldsymbol{\lambda}_{\hat{dq}}^{a}|^2} \quad \Rightarrow \quad K_{ag}(s) = 1. \tag{45}$$

The adaptive-gain to satisfy the condition $\boldsymbol{G}\,\boldsymbol{\lambda}_{\hat{dq}}^{a} = 0$ is given by

$$\boldsymbol{G} = \begin{bmatrix} k_1 \\ k_2 \end{bmatrix}\frac{\left(\boldsymbol{\lambda}_{\hat{dq}}^{a}\right)^{\mathrm{T}}}{|\boldsymbol{\lambda}_{\hat{dq}}^{a}|^2}\,\mathbf{J} \tag{46}$$

where k_1 and k_2 are the additional degrees of freedom to design the locus of the flux observer poles. For comparison with former schemes, the poles are placed at $s = -g \pm \omega$ as

$$\det\left(s\,\mathbf{I} + \boldsymbol{G} + \omega\mathbf{J}\right) = (s+g)^2 + \omega^2. \tag{47}$$

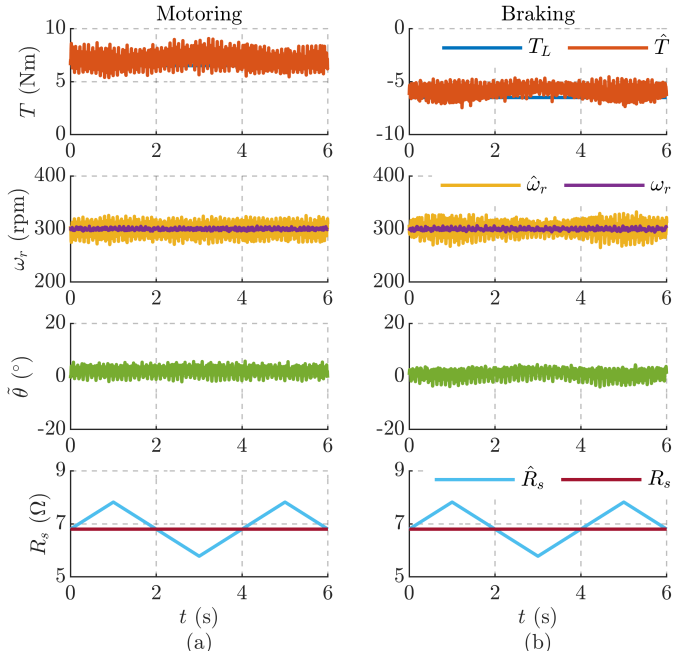

Fig. 15. APP position observer stability analysis with resistance perturbation of ±15% error, $\tilde{R}_s = \pm 0.15\, R_s$ at 300 rpm (0.2 p.u.) and rated torque: (a) Motoring; (b) Braking.

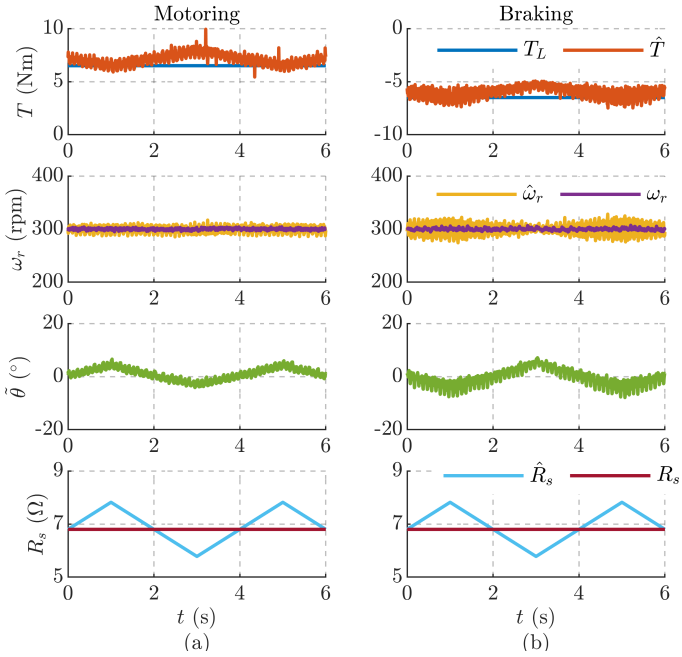

Fig. 16. AG position observer stability analysis with resistance perturbation of ±15% error, $\tilde{R}_s = \pm 0.15\, R_s$ at 300 rpm (0.2 p.u.) and rated torque: (a) Motoring; (b) Braking.

Solving, the gains are given by

$$\begin{bmatrix} k_1 \\ k_2 \end{bmatrix} = \frac{g}{\omega} \begin{bmatrix} g & 2\omega \\ -2\omega & g \end{bmatrix} \boldsymbol{\lambda}^{a}_{\hat{dq}}. \tag{48}$$

The locus of poles for the adaptive-gain approach are shown in Fig. 13(c). It can be observed that the poles are coincident with the design parameter, unlike the APP, due to dynamic decoupling of the two observers.

2) Experimental Results: The experimental validation of AG position observer under control resistance perturbation at rated torque and 300 rpm in Fig. 16 shows that the system is stable for motoring and braking operations although the position error is susceptible to the resistance variations.

V. Conclusions

The paper reviewed six flux observer-based sensorless techniques using a general mathematical framework. Each scheme was represented by a unique projection vector and was subjected to a common stability analysis to identify the operational limits under similar operating conditions.

Regions of instability were identified for CP scheme at low speeds braking and at high speeds flux-weakening operation. The AF scheme is found to be unstable at low speeds braking and high speeds flux weakening operation while the FS scheme is unstable at low speeds motoring operation. The latter three schemes (AUX, APP and AG) are stable at all operating points. APP scheme has an unique advantage of resistance immunity while AG scheme has decoupled flux and position observers with poles at the designated location. The results of the stability analysis were experimentally validated with a control resistance perturbation test on a 1.1 kW SyR machine test-bench.

References

[1] P. L. Jansen and R. D. Lorenz, "Transducerless position and velocity estimation in induction and salient AC machines," *IEEE Transactions on Industry Applications*, vol. 31, no. 2, pp. 240–247, 1995.

[2] C. E. Hwang, Y. Lee, and S. K. Sul, "Analysis on position estimation error in position-sensorless operation of IPMSM using pulsating square wave signal injection," *IEEE Transactions on Industry Applications*, vol. 55, no. 1, pp. 458–470, 2019.

[3] M. Schroedl and P. Weinmeier, "Sensorless control of reluctance machines at arbitrary operating conditions including standstill," *IEEE Transactions on Power Electronics*, vol. 9, no. 2, pp. 225–231, 1994.

[4] A. Varatharajan, P. Pescetto, and G. Pellegrino, "Sensorless Synchronous Reluctance Motor Drives: A Full-Speed Scheme using Finite-Control-Set MPC in a Projection Vector Framework," *IEEE Transactions on Industry Applications*, vol. 56, no. 4, pp. 3809–3818, 2020.

[5] J.-I. Ha, S.-J. Kang, and S. K. Sul, "Position-controlled synchronous reluctance motor without rotational transducer," *IEEE Transactions on Industry Applications*, vol. 35, no. 6, pp. 1393–1398, 1999.

[6] E. Capecchi, P. Guglielmi, M. Pastorelli, and A. Vagati, "Position-sensorless control of the transverse-laminated synchronous reluctance motor," *IEEE Transactions on Industry Applications*, vol. 37, no. 6, pp. 1768–1776, 2001.

[7] A. Yousefi-Talouki, P. Pescetto, and G. Pellegrino, "Sensorless Direct Flux Vector Control of Synchronous Reluctance Motors Including Standstill, MTPA, and Flux Weakening," *IEEE Transactions on Industry Applications*, vol. 53, no. 4, pp. 3598–3608, 2017.

[8] T. Hanamoto, H. Ikeda, T. Tsuji, and Y. Tanaka, "Sensorless speed control of synchronous reluctance motor using RTLinux," in *Proceedings of the Power Conversion Conference-Osaka 2002 (Cat. No.02TH8579)*, vol. 2, 2002, pp. 699–703 vol.2.

[9] I. Boldea, M. C. Paicu, G. Andreescu, and F. Blaabjerg, ""Active Flux" DTFC-SVM Sensorless Control of IPMSM," *IEEE Transactions on Energy Conversion*, vol. 24, no. 2, pp. 314–322, 2009.

[10] S. C. Agarlita, I. Boldea, and F. Blaabjerg, "High-frequency-injection-assisted 'active-flux'-based sensorless vector control of reluctance synchronous motors, with experiments from zero speed," *IEEE Transactions on Industry Applications*, vol. 48, no. 6, pp. 1931–1939, 2012.

[11] F. J. Barnard, W. T. Villet, and M. J. Kamper, "Hybrid Active-Flux and Arbitrary Injection Position Sensorless Control of Reluctance Synchronous Machines," *IEEE Transactions on Industry Applications*, vol. 51, no. 5, pp. 3899–3906, 2015.

[12] P. Landsmann, R. Kennel, H. W. De Kock, and M. J. Kamper, "Fundamental saliency based encoderless control for reluctance synchronous machines," *19th International Conference on Electrical Machines, ICEM 2010*, 2010.

[13] A. Varatharajan, G. Pellegrino, and E. Armando, "Sensorless synchronous reluctance motor drives: Auxiliary flux based position observer," *IEEE Journal of Emerging and Selected Topics in Power Electronics*, pp. 1–1, 2020.

[14] A. Varatharajan and G. Pellegrino, "Sensorless Synchronous Reluctance Motor Drives: A General Adaptive Projection Vector Approach for Position Estimation," *IEEE Transactions on Industry Applications*, vol. 56, no. 2, pp. 1495–1504, 2020.

[15] A. Varatharajan and G. Pellegrino, "Sensorless synchronous reluctance motor drives: A projection vector approach for stator resistance immunity and parameter adaptation," *IEEE Transactions on Industry Applications*, pp. 1–1, 2020.

[16] M. Hinkkanen, S. E. Saarakkala, H. A. A. Awan, E. Mölsä, and T. Tuovinen, "Observers for Sensorless Synchronous Motor Drives: Framework for Design and Analysis," *IEEE Transactions on Industry Applications*, vol. 54, no. 6, pp. 6090–6100, 2018.

[17] T. Tuovinen, H. A. A. Awan, J. Kukkola, S. E. Saarakkala, and M. Hinkkanen, "Permanent-Magnet Flux Adaptation for Sensorless Synchronous Motor Drives," in *2018 IEEE 9th International Symposium on Sensorless Control for Electrical Drives (SLED)*, 2018, pp. 138–143.

[18] S. Morimoto, K. Kawamoto, M. Sanada, and Y. Takeda, "Sensorless control strategy for salient-pole PMSM based on extended EMF in rotating reference frame," *IEEE Transactions on Industry Applications*, vol. 38, no. 4, pp. 1054–1061, 2002.

[19] Y. Inoue, Y. Kawaguchi, S. Morimoto, and M. Sanada, "Performance Improvement of Sensorless IPMSM Drives in a Low-Speed Region Using Online Parameter Identification," *IEEE Transactions on Industry Applications*, vol. 47, no. 2, pp. 798–804, 2011.

[20] Y. Lee and S. K. Sul, "Model-Based Sensorless Control of an IPMSM With Enhanced Robustness Against Load Disturbances Based on Position and Speed Estimator Using a Speed Error," *IEEE Transactions on Industry Applications*, vol. 54, no. 2, pp. 1448–1459, 2018.

[21] H. Kim, J. Son, and J. Lee, "A High-Speed Sliding-Mode Observer for the Sensorless Speed Control of a PMSM," *IEEE Transactions on Industrial Electronics*, vol. 58, no. 9, pp. 4069–4077, 2011.

[22] S. Bolognani, L. Tubiana, and M. Zigliotto, "EKF-based sensorless IPM synchronous motor drive for flux-weakening applications," *IEEE Transactions on Industry Applications*, vol. 39, no. 3, pp. 768–775, 2003.

[23] D. Liang, J. Li, and R. Qu, "Sensorless Control of Permanent Magnet Synchronous Machine Based on Second-Order Sliding-Mode Observer With Online Resistance Estimation," *IEEE Transactions on Industry Applications*, vol. 53, no. 4, pp. 3672–3682, 2017.

[24] A. Piippo, M. Hinkkanen, and J. Luomi, "Analysis of an Adaptive Observer for Sensorless Control of Interior Permanent Magnet Synchronous Motors," *IEEE Transactions on Industrial Electronics*, vol. 55, no. 2, pp. 570–576, 2008.

[25] M. Hinkkanen, T. Tuovinen, L. Harnefors, and J. Luomi, "A Combined Position and Stator-Resistance Observer for Salient PMSM Drives: Design and Stability Analysis," *IEEE Transactions on Power Electronics*, vol. 27, no. 2, pp. 601–609, 2012.

[26] E. Armando, R. I. Bojoi, P. Guglielmi, G. Pellegrino, and M. Pastorelli, "Experimental identification of the magnetic model of synchronous machines," *IEEE Transactions on Industry Applications*, vol. 49, no. 5, pp. 2116–2125, 2013.